Title: Rapid root growth brake by TIR1 auxin signaling

Supplementary Material

Contents

Supplementary Text: 1
Supplementary Figures 7
Supplementary Tables 12
Supplementary References 16

Supplementary Text:

Model of IAA transport from media into the root

1. Model description

To assess temporal dynamics of intracellular auxin accumulated from the media into the elongating root cells, we simulated auxin transport in the root tip. Our model follows the framework used in the previous models of auxin transport[12–14]: root tip comprises a multicellular structure with isolated intracellular compartments and extracellular compartment (the cell wall), within which auxin can diffuse freely. Auxin transport between the adjacent compartments is governed by its concentration gradient and membrane permeability. There are three distinct paths for auxin molecule to permeate the cell membrane: diffusion, influx carriers and efflux carriers. As shown previously, major governing factor for auxin transport is the distribution of membrane permeabilities for auxin through these paths, which depend on localization of the carrier proteins (AUX1, PINs and others)[12–14]. Our model contains also a media compartment around the root to simulate external auxin concentration.

Model Geometry

Presenting the root tip as an array of rectangular cells has computational advantages and provided useful quantitative results in the past[12,14,15]. We draw 2D rectangular geometry of the half of a root tip, containing cells of the root apex: meristematic zone, elongation zone and the beginning of the differentiation zone (where cells are no longer elongating) (Fig. S4A). Total root geometry is~ 1500µm in length, 80µm in width. Right outmost domain represents media. As auxin distribution depends on individual cell sizes[14], it is crucial to recapitulate cellular dimensions as close to the real root as possible. Most important is to preserve the cell volume distribution in the real root. To fulfill this requirement and facilitate assigning of membrane permeabilities in the same time, the widths of the cell files in our model correspond to those in elongation zone, taken from segmented confocal images[16]. The heights of the cells are also taken from segmented confocal images. Lateral root cap is drawn as an additional cell file on the outer side of meristematic zone. Cell wall thickness is set to 200 nm.

The 3D structure is obtained by rotating 2D geometry around the central axis. Assuming auxin concentrations and dynamics to be axisymmetric (neglecting variations around the roots circumference) enables us to capture the 3D structure of the root tip without significantly increasing simulation time. However, this approach eliminates lateral cell membranes, which are parallel to the rotating plane (perpendicular to the circumference). In our model we compensate for these missing membranes by proportional increase in permeability of the rest of the cell contour.

Parameters governing auxin transport; specifying the carrier distributions.

Bulk diffusion. Diffusion coefficients inside the cell and in the media are assumed to be equal to diffusion in water at the room temperature $D_c = D_m = 600\ \mu m^2/s$ [12]; in the wall $D_w = 32\ \mu m^2/s$ based on measurements [17].

Carrier distribution. Membrane transport of auxin has three components: 1) diffusion of the IAAH, protonated form of auxin, 2) influx of anion IAA^- from the wall into the cell via influx carriers, 3) efflux of IAA^- from the cell into the wall via efflux carriers. Diffusional permeability is the same for all cell boundaries. Carrier-mediated membrane permeabilities depend on carrier density and on the specific permeability of the unit density of a carrier. Carrier densities are assigned for each cell boundary following the carrier localization schemes presented in *Simuplant,* default settings[16]: based on the fluorescence staining of the main known auxin transporters in the root (AUX1, LAX2 and LAX3 influx transporters; PIN1, PIN2, PIN3, PIN4 and PIN7 efflux transporters) it has been assumed that either carrier is present on the membrane and its density equals 1 or it is absent with the density equal 0 (Fig. S4A). Most cells containing influx carriers have them localized on all sides of the cell membrane[13]. AUX1 is localized mostly in outward cell layer: lateral root cap (LRC) and epidermis (Fig.3B, Fig. S4A). PIN proteins are polarized in most cells (QC is an exception, where PINs are on all boundaries) and each cell has the prevailing PIN type expressed. This results in the characteristic distribution of PINs within the root[13], proved to cause the reverse auxin fountain: the downward auxin flux in the stele and upward auxin flux in the outer cell layer[14]. Other non-polar efflux transporters (NPEs) are not yet characterized well, but they are not polarized as PINs and are thought to have much less permeability[16]. In the main model we neglect non-polar efflux carriers (NPEs), but sensitivity of the solution for their presence on all cell boundaries is calculated (Table S2). We simulate *aux1* mutant lacking AUX1 carrier by setting AUX1 density to 0 in the outer layer (epidermis and LRC).

Measured permeability values. Permeability values have been measured separately for diffusion, influx and efflux carriers in a number of studies[18,19]. Rutschow et al. provide diffusion permeability for Arabidopsis root protoplasts ($P_{IAAH} = 0.35 \pm 0.22\ \mu m/s$), which is close to the values provided by[19] for tobacco cells. Influx permeability in AUX1-positive root protoplasts was determined[18] as: $P_{AUX1} = 0.35 \pm 0.07 \mu m/s$. We assume $P_{LAX2,3} = P_{AUX1}$ [13]. Permeability for PINs has been previously estimated as ~ $0.3 \mu m/s$ [12]. One way to estimate the PIN efflux permeability in epidermis is from the auxin transport velocity in the shoot direction, that corresponds to polar transport[19]. Measured auxin velocities in the Arabidopsis root are in the range of $0.3 \div 3 \mu m/s$ [20]. To get upward auxin flux in the epidermis ~ $1\ \mu m/s$ in our model, we set the efflux permeability of PIN2, which is polarized shootward in epidermis and solely defines the shootward IAA transport: $P_{PIN2} = 0.5 \pm 0.2 \mu m/s$. This is close to the value estimated by[18]. We assume that all PINs-containing cells have the same P_{PIN} disregarding the PIN type and number of different PINs. This assumption is rough, however, as we aim to calculate $[IAA]_{cell}$ mainly in epidermis, we choose P_{AUX1} and P_{PIN2} to be the reference values.

Other assumptions:
(i) Saturation of the auxin transporters is not considered, because concentrations tested in the model are below saturation level: $K_{D(AUX1)} \cong 2\mu M$, $K_{D(PINs)} \cong 6\mu M$ [21], whereas 1nM≤$[IAA]_{ext}$≤50nM and calculated $[IAA]_{cell} < 3\mu M$.
(ii) Auxin synthesis and degradation are neglected in the model. It is not known precisely, what is auxin synthesis rate in the root and what fraction of auxin present in the root is transported from the shoot. Nevertheless, E. Kramer and E. Ackelsberg estimated that synthesis contributes to less than 1% of the auxin amount present in the fast transporting tissues such as root[22]. Auxin degradation is also a slow process compared to transport[16,22]. As we have an infinite pool of auxin (coming from shoot and media), degradation can be assumed negligible.

For the complete list of the parameters used in the model see Tables S2 and S3.

Equations for diffusion within compartments and membrane auxin fluxes.

Dynamic auxin distribution is calculated by solving a system of Partial Differential Equations (PDEs) that describe how the auxin concentration IAA(x,t) within each compartment evolve due to bulk auxin diffusion (Fick's law) and mass conservation law:

$$\frac{\partial [IAA]_{c/w/m}}{\partial t} = D_{c/w/m} \cdot \Delta [IAA]_{c/w/m}. \quad \text{(Eq.1.)}$$

Normal diffusive auxin flux at the boundaries of compartments equals to auxin flux across membrane between compartments:

$$J_{boundary} = -D_{c/w/m} \cdot \nabla [IAA]_{c/w/m} = J_{through\ PM}$$

(=molecules passed through membrane per unit time per unit area), which is governed by membrane permeabilities:

$$J_{wall \to cell} = J_{diff} + J_{influx} + J_{efflux}\ , \quad \text{(Eq.2)}$$
$$J_{diff} = P_{IAAH}(A_1 \cdot [IAA]_{wall} - B_1 \cdot [IAA]_{cell}) \quad \text{(Eq.3)}$$
$$J_{influx} = P_{AUX1\ or\ LAX2,3}(A_2 \cdot [IAA]_{wall} - B_2 \cdot [IAA]_{cell}) \quad \text{(Eq.4)}$$
$$J_{efflux} = P_{PIN}(A_3 \cdot [IAA]_{wall} - B_3 \cdot [IAA]_{cell}), \quad \text{(Eq.5)}$$

where A_i, B_i are coefficients that depend on pH_{wall}, pH_{cell}, pK of auxin and membrane potential V_m. Total IAA concentration is a sum of protonated form and anion form: $[IAA] = IAAH + IAA^-$. Expressions for A_i, B_i account for IAAH and IAA^- ratio in solution due to pH and also for electric potential gradient across the membrane (Fig. S4B). Derivation of A_i, B_i is provided in detail in[16] and[12]. For $pH_{wall} = 5.3$, $pH_{cell} = 7.2, V_m = -120mV$, typical for the root, these constants have the following values:

$$J_{diff} = P_{IAAH}(0.24 \cdot [IAA]_{wall} - 0.004 \cdot [IAA]_{cell}) \quad \text{(Eq.3')}$$
$$J_{influx} = P_{AUX1\ or\ LAX2,3}(3.57 \cdot [IAA]_{wall} - 0.045 \cdot [IAA]_{cell}) \quad \text{(Eq.4')}$$
$$J_{efflux} = P_{PIN}(0.034 \cdot [IAA]_{wall} - 4.68 \cdot [IAA]_{cell}), \quad \text{(Eq.5')}$$

Numerical procedure
PDEs are solved in finite element software Comsol Multiphysics 5.2a: domains of the 2D geometry are discretized by constructing a mesh of 41702 triangular elements. Variables are defined in vertices and computed over time. Time steps are determined by solver.

External boundary conditions (Fig.S4A). On the upper boundary of the stele the IAA concentration is set to constant C_{shoot}, that corresponds to the supply of auxin from the shoot.

On the upper boundary of the epidermis the sink is set also by IAA concentration condition: C_{epi}=0. The external boundary of the media compartment has concentration equal to applied auxin: C_{ext}=IAA_{ext}. The rest of the external boundaries have "no flux" boundary condition. We tested that auxin accumulation into epidermal cells from the media doesn't depend on C_{epi} because it is governed by concentration in the media and the upward flux by PINs. To define C_{shoot} we take into account the average [IAA] in the intact root tip of 1mm length, which has been experimentally found to be ~200nM[23,24]. C_{shoot} =400nM gives the same average [IAA] without auxin application (C_{ext}=0).

Initial conditions. First, we calculate steady state solution for the C_{ext}=0 (Fig. S4C): this endogenous $[IAA]_{cell}$ and $[IAA]_{wall}$ distribution in the root serves as initial conditions for further numerical analysis of IAA accumulation (for Fig. S4D-H). The initial auxin concentration in epidermis before auxin application is $[IAA]_{cell0}$~=5nM in the control and $[IAA]_{cell0}$~=1.4nM in *aux1*.

Starting from initial concentrations our model calculates $[IAA]_{cell}$ and $[IAA]_{wall}$ change in time due to accumulation and eventually comes to constant: a *steady state* solution. In a steady state net fluxes through membranes are also constant, but not zero: auxin can be pumped into the cell at one boundary and pumped out at the other boundary while keeping $[IAA]_{cell}$ constant.

2. Results

Control

We use the model to calculate steady state and temporal dependence of the auxin accumulation after application of $[IAA]_{ext}$. Cell-average $[IAA]_{cell}$ in epidermal cells rises after external auxin application and establishes an ascendant gradient along the elongation zone because auxin is pumped up by efflux carriers (Fig.S4E). We will further present $[IAA]_{cell}$ for the 5th epidermal cell above the lateral root cap for simplicity (see Fig.S4E,F), as its value correspond to the volume-average $[IAA]_{cell}$ of all epidermal cells in the elongation zone.

For 1nM<$[IAA]_{ext}$ <50nM auxin steady state accumulation can be described by a single parameter: $\alpha=[IAA]_{cell}/[IAA]_{ext}$ – accumulation ratio (Fig.S4DE). In control α^{Col}~=30±12 (error is due to parameter variation (Table S2) and to slight difference for different $[IAA]_{ext}$ (Fig.S4D)).

From α^{Col} and experimental IC_{50} that causes half growth inhibition we can find the intracellular auxin concentration that causes half growth inhibition, namely $IAA_{cell50}^{col} = \alpha^{col} \cdot IC_{50}^{col} = 43 \pm 18nM$. Assuming that *tir triple* mutant accumulates IAA as much as the control, one can calculate auxin concentration that causes half growth inhibition when there are not enough receptors present: $IAA_{cell50}^{tir} = \alpha^{col} \cdot IC_{50}^{tir} = 275 \pm 115nM$. It gives an estimate of affinity between TIR1/ABF-Aux/IAA and auxin given that it is a primary receptor in the growth inhibition pathway[25]. Affinities measured for some of the TIR1/ABF-Aux/IAA pairs indeed fall in this range[26].

Temporal dynamics of auxin accumulation is shown on Fig.S4E: time to reach half maximum concentration $t_{1/2}$~=150s. ($t_{1/2}$~= 60s to 200s depending on cell location and on parameter variation as shown in Fig.3G.) It is instructive to estimate t_{IC50} - time to reach intracellular concentration $IAA_{cell50}^{col} = \alpha^{col} \cdot IC_{50}^{col}$, that causes half growth inhibition. (This time doesn't depend on α^{Col}, which acts as a common scale factor for both half inhibitory concentration and for the steady state concentration.) Comparison of t_{IC50} to the half inhibition time of GR, τ_{GR50}, provides information about timing for signaling cascade. Even for $[IAA]_{ext}$=5nM t_{IC50}~*70sec* is much shorter than $\tau_{GR50} = 6min$, giving an estimate of *5min* characteristic time

for the full response execution (reaching *responseGR*). At higher $[IAA]_{ext}$, IAA_{cell50}^{col} is reached faster, and thus reduces the total response time, which is consistent with experimental data for $[IAA]_{ext}$=50nM. We conclude, that auxin uptake alone cannot explain temporal dependence of GR inhibition, and that signaling pathway should contain few fast reaction steps.

Influx mutant *aux1*

Auxin accumulation ratio α^{aux1}~=1.9±0.5, that gives

$$\frac{\alpha^{col}}{\alpha^{aux1}} = 15.9 \pm 5.5 \qquad \text{(Eq.6.)}$$

$[IAA]_{cell}$ in *aux1* reaches steady state faster than in the control: $t_{1/2}$~=100s (Fig.S4G).

Notes on assumption of zero influx permeability in aux1. Measurements of auxin fluxes in the null mutant *aux1*-22 show, that it's influx permeability can be up to 15% of that in control[18]. If we account for such influx carrier activity in the *aux1* mutant (in the outer cell layer), we get $\frac{\alpha^{col}}{\alpha^{aux1}} = 6$ in our model. Thus, influx permeability in the mutant, if present, reduces difference between control and *aux1* and makes it lower than the experimental value. It is possible, however, that non-zero influx in *aux1*-22 in those experiments is caused by LAX transporters, that are not present in epidermis. Thus, epidermal cells, which are the focus of our analysis, can indeed have no influx activity in *aux1*. In our experiments we use *aux1*-100, which is also null mutant, but for which no permeability measurements are available. Not having more precise experimental values, we assume that influx permeability in the outer cell layer of *aux1* mutant is lowest possible: $P_{AUX1} = 0$.

Sensitivity of accumulation ratios on parameter variations is presented in Table S2. Changing permeability values within the range of their standard deviations gives maximum error of the solution, presented in the Table S4.

Simplified 1D model to estimate ratio between control and *aux1* accumulation $\alpha^{Col}/\alpha^{aux1}$

Auxin accumulation ratio in epidermis in our numerical model depends only slightly on the transport properties of the other cells composing the root. Thus, considering these cells in the model doesn't change the result much. We can simplify our model even further and not account for PIN polarity, assuming that efflux carriers are distributed around the epidermal membrane evenly. Then the steady state concentration can be found simply from the balance of the auxin fluxes across any segment of the membrane:

$$J_{wall\to cell} = J_{diff} + J_{influx} + J_{efflux} = 0 \qquad \text{(Eq.7.)}$$

From Eq.3'-5 ' in control:

$$\alpha^{col} = \frac{[IAA]_{cell}}{[IAA]_{wall}} = \frac{P_{IAAH}\cdot 0.24 + P_{AUX1}\cdot 3.57 + P_{PIN}\cdot 0.034}{P_{IAAH}\cdot 0.004 + P_{AUX1}\cdot 0.045 + P_{PIN}\cdot 4.6}, \qquad \text{(Eq.8.)}$$

and in *aux1* ($P_{AUX1} = 0$):

$$\alpha^{aux1} = \frac{[IAA]_{cell}}{[IAA]_{wall}} = \frac{P_{IAAH}\cdot 0.24 + 0 + P_{PIN}\cdot 0.034}{P_{IAAH}\cdot 0.004 + 0 + P_{PIN}\cdot 4.6}. \qquad \text{(Eq.9.)}$$

Introducing values of permeabilities (Table S2) allows to approximate:

$$\frac{\alpha^{col}}{\alpha^{aux1}} = \frac{P_{IAAH}\cdot 0.24 + P_{AUX1}\cdot 3.57}{P_{PIN}\cdot 4.6} \cdot \frac{P_{PIN}\cdot 4.6}{P_{IAAH}\cdot 0.24} = 13.3 \pm 3.5 \qquad \text{(Eq.10.)}$$

In this simple model ratio between control and *aux1* doesn't depend on efflux permeability, which is cancelled, but solely on the diffusive and influx permeabilities, that are measured in

the root quite precisely[18]. We conclude, that the root geometry and PIN polarity only slightly contribute to the observed difference between control and *aux1* growth inhibition.

II. Fitting procedures

Calculation of response growth rate from experimental growth curves.
We normalize growth inhibition curves by the growth rate immediately preceding auxin application (*initGR*). Using MATLAB, we fitted individual normalized growth inhibition curves with an exponentially descending function that gives us the steady state growth rate, reached by the root after a while: *responseGR*. At high $[IAA]_{ext}$ *responseGR* saturates: roots do not fully stop; the minimal responseGR, GR_{min}, is about 13% in control (consistent with previous reports[27]). Surprisingly, we didn't find any correlation between *initGR* and GR_{min}: fast roots that grow at *initGR*~7 μm/min reduce their growth rate to 13% as well as slow roots with *initGR*~1 μm/min. Nor we observed any correlation between *initGR* and *responseGR* for any $[IAA]_{ext}$. Thus, normalization to *initGR* is justified.

Hill-equation fit of *responseGR*. Dependence of *responseGR* on the dose, $\log_{10}([IAA]_{ext})$, has sigmoidal shape, characteristic for dose-effect curves (Fig.1E, Fig.3D, Fig.4B). Dose-effect curves are usually fitted by Hill equation[28]. For normalized *GR* equation takes the form:

$$GR([IAA]_{ext}) = \frac{1-GR_{min}}{1+\left(\frac{[IAA]_{ext}}{IC_{50}}\right)^{k}} + GR_{min}, \qquad \text{(Eq.12)}$$

where maximum growth rate equals 1, GR_{min} is minimal growth rate, IC_{50} is half inhibitory concentration of $[IAA]_{ext}$ and k characterizes steepness of the slope.
Fitting was performed in MATLAB. Fitted coefficient values are listed in Table S1.

Theoretical growth rate response (Fig.3H). We use the same Hill equation to predict growth inhibition in time on the assumption that cells react instantaneously to the $[IAA]_{cell}$ reached at the moment:

$$GR^{i}(t) = \frac{1-GR_{min}}{1+\left(\frac{[IAA]^{i}_{cell}(t)}{\alpha^{i} \cdot IC^{i}_{50}}\right)^{k}} + GR_{min}\,, \qquad \text{(Eq.12)}$$

where i=control, *aux1*.
GR_{min}, k, α^{i}, IC^{i}_{50} values are listed in Tables S1 and S4. Calculated $GR^{i}(t)$ are shown in Fig.3H for $[IAA]_{ext}$=5nM and $[IAA]_{ext}$=50nM. Fig.3H illustrates difference between reaction to particular $[IAA]_{ext}$ in control and *aux1*. It also shows that for higher $[IAA]_{ext}$ GR inhibition should become more steep and the curve becomes more asymmetric: inhibition and resumption parts are symmetric only when steady state $[IAA]_{cell}$ doesn't considerably exceed the half maximal inhibitory concentration. That is why curves for *aux1* are more symmetric than for control, which accumulates much more.

Notably, the slopes of all theoretical curves are steeper than experimental GR(t), indicating that a delay between signaling and the execution of the response is present also in *aux1*.

Supplementary Figures

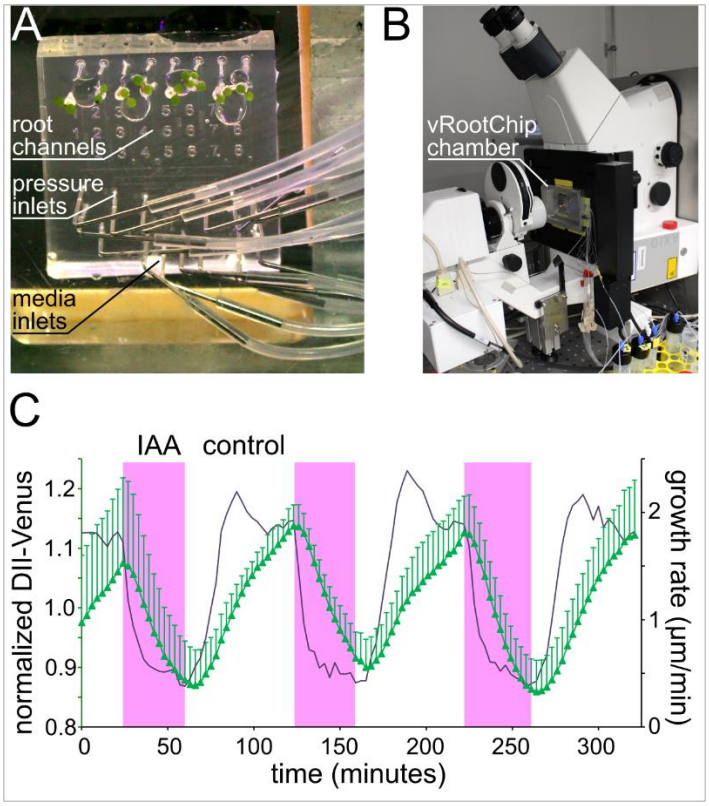

Fig. S1. A) Photo of vRootChip with Arabidopsis seedlings and connected tubing for pressure control and media influx. B) Photo of the assembled vRootChip device on the vertical confocal microscope. C) DII-Venus intensity dynamics (green line) during a repetitive treatment with 10nM IAA is closely correlated with the growth rate dynamics (black line, the same data as in Fig.1F). DII-Venus was measured in the lateral root cap and stele, and was normalized to the mean value over the course of the experiment for each root. Mean intensity of 8 roots +SD.

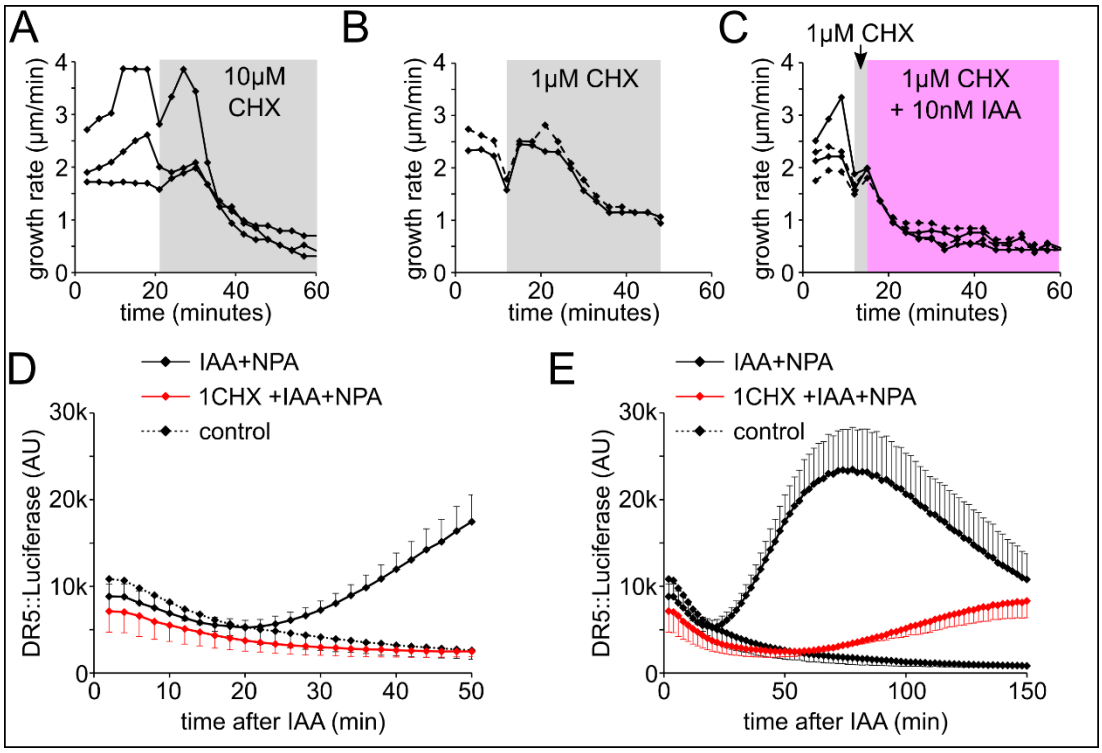

Fig. S2. A) Effect of 10µM cycloheximide (shaded in grey) on root growth of three individual roots. B) Effect of 1µM cycloheximide (shaded in grey) on root growth of two individual roots. C) Pretreatment with 1µM cycloheximide (grey) does not prevent the IAA-triggered (magenta) root growth inhibition. Time course of four individual roots. D) Addition of 1µM cycloheximide inhibits the IAA-triggered increase in DR5::luciferase intensity (D). After 50 minutes, DR5::luciferase starts to be expressed due to dilution of the inhibitor into the medium (E). The data of control and IAA+NPA correspond to Figure 2EF, and represent the mean ±SD of 5 root tips for each condition; D is a zoom of E.

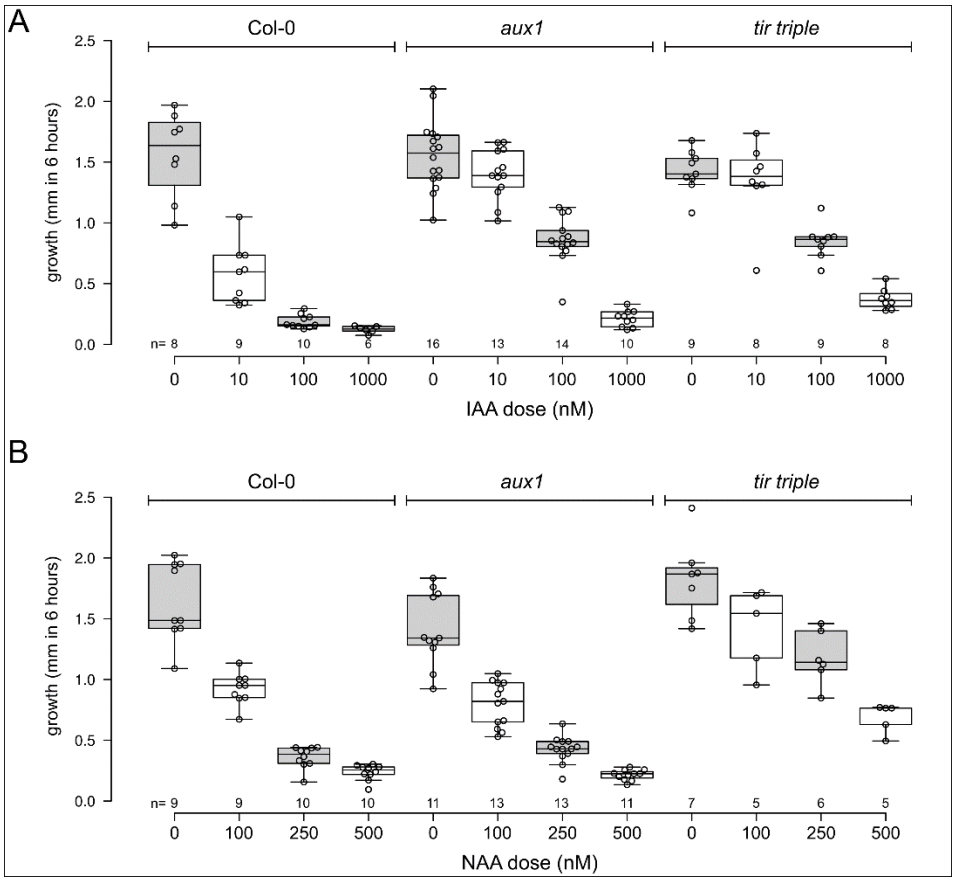

Fig. S3. A,B) Growth of control Col-0, *aux1* and *tir triple* mutant roots on the surface of media supplemented with increasing concentration of IAA or NAA. Growth was measured as the displacement of the root tip during a six-hour experiment. In the boxplots, center lines show the medians; box limits indicate the 25th and 75th percentiles as determined by R software; whiskers extend 1.5 times the interquartile range from the 25th and 75th percentiles, individual datapoints are represented by dots, n is indicated below each boxplot.

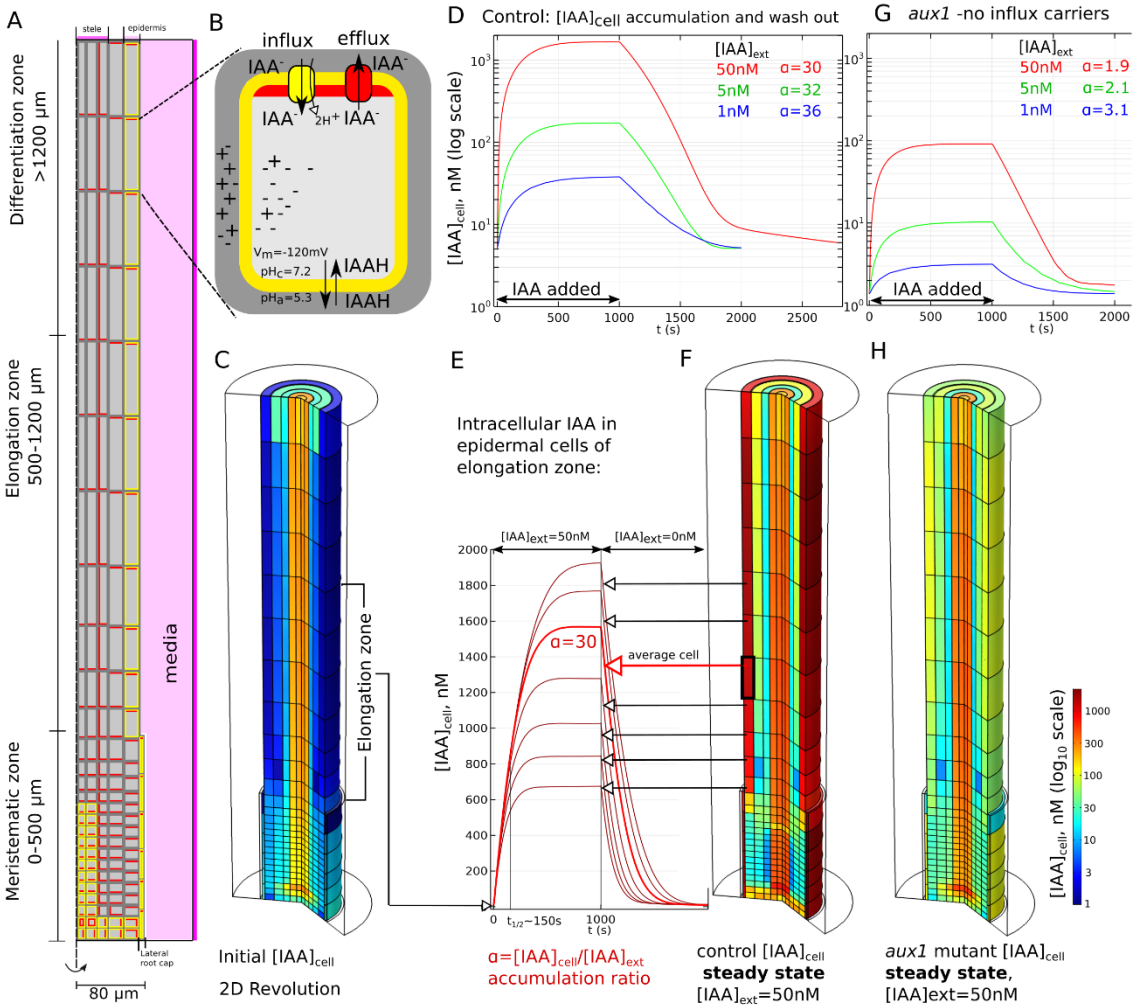

Fig. S4. A) Model geometry: intracellular domains (light gray), cell wall domain (dark gray), media (magenta). Magenta lines indicate boundaries with auxin concentration condition. Localization of influx (yellow) and efflux (red) transporters. B) Scheme of one cell showing three paths for IAA transport through membrane, that determine IAA flux. C) IAA concentration in the modeled root at $[IAA]_{ext} = 0$, that is used as initial condition in D. Scale bar in the right low corner is the same for C,F,H. D) Control root $[IAA]_{cell}$ accumulation for different $[IAA]_{ext}$ and wash out upon $[IAA]_{ext}$ removal (log scale). E) $[IAA]_{cell}$ accumulation and removal in control for $[IAA]_{ext}$ =50nM, volume-average for individual cells of elongation zone. The 5th cell above LRC accumulates average $[IAA]_{cell}$ of all cells. F) Control steady state auxin pattern at $[IAA]_{ext}$ =50nM, reached at ~1000s. G) aux1 root $[IAA]_{cell}$ accumulation for different $[IAA]_{ext}$ and wash out upon $[IAA]_{ext}$ removal (log scale). H) *aux1* steady state auxin pattern at $[IAA]_{ext}$ =50nM, reached at ~500s.

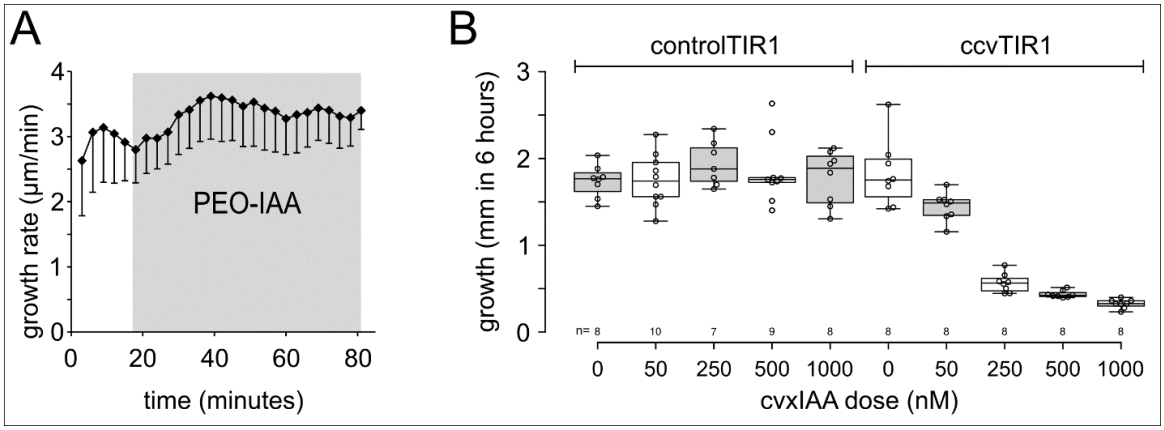

Fig. S5. A) PEO-IAA addition stimulates root growth. 5µM PEO addition is shaded grey. Mean of 9 roots, -SD. B) Growth of controlTIR1 and ccvTIR1 roots on medium with increasing concentrations of cvxIAA. Growth was measured as the displacement of the root tip during a six-hour experiment. In the boxplots, center lines show the medians; box limits indicate the 25th and 75th percentiles as determined by R software; whiskers extend 1.5 times the interquartile range from the 25th and 75th percentiles, individual datapoints are represented by dots, n is indicated below each boxplot.

Supplementary Tables

Table S1. Coefficients in Hill equations (Eq.12) fitted to experimental dose-response (Fig.1E, Fig.3D, Fig.4B), (±95% confidence bounds).

	IC_{50} , nM	GR_{min}	k
Control	1.44 (±0.23)	0.13 (±0.03)	1.63 (±0.43)
aux1	17.2 (±4.7)	0.14 (±0.03)	1.88 (±0.87)
tir triple	17.8 (± 2.01)	0	0.89 (±0.07)

Table S2. Permeability values and variation used in the model.

Parameter	**Value in the model, [µm/s]**	**Reference, reference value**	**Sensitivity of accumulation ratio α to permeabilities** [change in α per 0.1 µm/s]	
			α^{Col}=30.3	**α^{aux1}**=1.9
P_{AUX1} (permeability of influx carriers)	0.7±0.15 *	$P_{AUX1} \cdot A_2 = 1.5 \pm 0.3$ µm/s => $P_{AUX1} = 0.35 \pm 0.07\ \mu m/s$ (Rutschow et al., 2014)	5.96	0
P_{PIN} (permeability of PIN efflux carriers)	0.5±0.2 **	$P_{PIN} \cdot B_3 = 2\ \mu m/s$ => $P_{PIN} = 0.43\ \mu m/s$ (Rutschow et al., 2014)	-3.17	- 0.49
P_{IAAH} (diffusive permeability for IAAH)	0.8±0.4 *	$P_{IAAH} = 0.35 \pm 0.22\ \mu m/s$ (Rutschow et al., 2014)	0.226	0.5
P_{NPE} (permeability of non-PIN-efflux carriers)	0	$P_{NPE} \leq 0.3 \cdot P_{PIN}$ (Band et al., 2014)	-149	- 2.88

* Permeabilities for influx carriers and diffusion are 2 times higher than the reference value to account for the lateral membranes, not included in the model geometry, which have area approximately equal to the area of membranes present in the model and also have the same permeabilities (Fig.S15C in (Band et al., 2014)).

** Efflux permeability doesn't account for the lateral membranes because efflux transporters are not present on these membranes.

Table S3. Other parameter values used in the model.

Parameter	**Value**	**Reference**
pH_{cell}	5.3	(Band et al., 2014)
pH_{wall}	7.2	(Band et al., 2014)
pK (IAA dissociation constant)	4.8	(Band et al., 2014)
D_c (IAA diffusion in cell)	$600\ \mu m^2/s$	(Swarup et al., 2005)
D_m (IAA diffusion in media)	$600\ \mu m^2/s$	(Swarup et al., 2005)
D_w (IAA diffusion in wall)	$32\ \mu m^2/s$	(Kramer et al., 2007)
V_m (membrane potential)	-120 mV	(Band et al., 2014)
Cell wall thickness	$0.2\ \mu m$	rounded from (Band et al., 2014)

Table S4. Accumulation ratios $\alpha=[IAA]_{cell}/[IAA]_{ext}$ for Control and *aux1* mutant , ± maximum variation based on variation of permeability values (see Table S2).

	3D numerical model	**simple 1D model, not accounting for PIN polarity**	**$(IC_{50}^{aux1})/(IC_{50}^{Col})$ from experimental fit (±95% confidence bounds)**
control α^{Col}	30.3 ±12.5	5.3 ±2.5	
aux1 α^{aux1}	1.9 ±0.5	0.4 ±0.2	
$\alpha^{Col}/\alpha^{aux1}$	**15.9 ± 5.5**	**13.3 ± 3.5**	**11.8 ± 3.77**

Supplementary References

1. Brunoud, G. *et al.* A novel sensor to map auxin response and distribution at high spatio-temporal resolution. *Nature* **482,** 103–6 (2012).
2. Moreno-Risueno, M. A. *et al.* Oscillating gene expression determines competence for periodic Arabidopsis root branching. *Science* **329,** 1306–11 (2010).
3. Swarup, R. *et al.* Structure-Function Analysis of the Presumptive Arabidopsis Auxin Permease AUX1. *Plant Cell* **16,** 3069–3083 (2004).
4. Dharmasiri, N. *et al.* Plant development is regulated by a family of auxin receptor F box proteins. *Dev. Cell* **9,** 109–119 (2005).
5. Uchida, N. *et al.* Chemical hijacking of auxin signaling with an engineered auxin–TIR1 pair. *Nat. Chem. Biol.* (2018). doi:10.1038/nchembio.2555
6. Grossmann, G. *et al.* Time-lapse Fluorescence Imaging of Arabidopsis Root Growth with Rapid Manipulation of The Root Environment Using The RootChip. *J. Vis. Exp.* e4290–e4290 (2012). doi:10.3791/4290
7. von Wangenheim, D. *et al.* Live tracking of moving samples in confocal microscopy for vertically grown roots. *Elife* **6,** (2017).
8. Li, L., Krens, S. F. G., Fendrych, M. & Friml, J. Real-time Analysis of Auxin Response, Cell Wall pH and Elongation in Arabidopsis thaliana Hypocotyls. *Bio-Protocol* **7,** 1–10 (2018).
9. P. Thévenaz, U.E. Ruttimann, M. U., Thevenaz, P., Ruttimann, U. E. & Unser, M. A Pyramid Approach to Subpixel Registration Based on Intensity. *IEEE Trans. Image Process.* **7,** 27–41 (1998).
10. Schneider, C. a, Rasband, W. S. & Eliceiri, K. W. NIH Image to ImageJ: 25 years of image analysis. *Nat. Methods* **9,** 671–675 (2012).
11. Schindelin, J. *et al.* Fiji: an open-source platform for biological-image analysis. *Nat. Methods* **9,** 676–682 (2012).
12. Swarup, R. *et al.* Root gravitropism requires lateral root cap and epidermal cells for transport and response to a mobile auxin signal. *Nat. Cell Biol.* **7,** 1057–1065 (2005).
13. Band, L. R. *et al.* Systems analysis of auxin transport in the Arabidopsis root apex. *Plant Cell* **26,** 862–875 (2014).
14. Grieneisen, V. A., Xu, J., Marée, A. F. M., Hogeweg, P. & Scheres, B. Auxin transport is sufficient to generate a maximum and gradient guiding root growth. *Nature* **449,** 1008–1013 (2007).
15. Van Den Berg, T., Korver, R. A., Testerink, C. & Ten Tusscher, K. H. W. J. Modeling halotropism: a key role for root tip architecture and reflux loop remodeling in redistributing auxin. *Development* **143,** 3350–3362 (2016).
16. Band, L. R. *et al.* Systems analysis of auxin transport in the Arabidopsis root apex. *Plant Cell* **26,** 862–875 (2014).
17. Kramer, E. M., Frazer, N. L. & Baskin, T. I. Measurement of diffusion within the cell wall in living roots of Arabidopsis thaliana. *J. Exp. Bot.* **58,** 3005–3015 (2007).
18. Rutschow, H. L., Baskin, T. I. & Kramer, E. M. The carrier AUXIN RESISTANT (AUX1) dominates auxin flux into Arabidopsis protoplasts. (2014).
19. Delbarre, A., Muller, P., Imhoff, V. & Guern, J. Comparison of mechanisms controlling uptake and accumulation of 2,4-dichlorophenoxy acetic acid, naphthalene-1-acetic acid, and indole-3-acetic acid in suspension-cultured tobacco cells. *Planta* **198,** 532–541 (1996).
20. Kramer, E. M., Rutschow, H. L. & Mabie, S. S. AuxV: a database of auxin transport velocities. *Trends Plant Sci.* **16,** 461–463 (2011).
21. Carrier, D. J. *et al.* The binding of auxin to the Arabidopsis auxin influx transporter AUX1. *Plant Physiol.* **148,** 529–35 (2008).

22. Kramer, E. M. & Ackelsberg, E. M. Auxin metabolism rates and implications for plant development. *Front. Plant Sci.* **6,** 150 (2015).
23. Band, L. R. *et al.* Root gravitropism is regulated by a transient lateral auxin gradient controlled by a tipping-point mechanism. *Proc. Natl. Acad. Sci. U. S. A.* **109,** 4668–4673 (2012).
24. Swarup, R. *et al.* Localization of the auxin permease AUX1 suggests two functionally distinct hormone transport pathways operate in the Arabidopsis root apex. *Genes Dev.* **15,** 2648–53 (2001).
25. Katzung, B. G. & Trevor, A. J. *Basic and clinical pharmacology*. (2012).
26. Calderón Villalobos, L. I. A. *et al.* A combinatorial TIR1/AFB-Aux/IAA co-receptor system for differential sensing of auxin. *Nat. Chem. Biol.* **8,** 477–85 (2012).
27. Evans, M. L. & Ishikawa, H. Responses of Arabidopsis roots to auxin studied with high temporal resolution : Comparison of wild type and auxin-response mutants. (1994).
28. Giraldo, J., Vivas, N. M., Vila, E. & Badia, A. Assessing the (a)symmetry of concentration-effect curves: Empirical versus mechanistic models. *Pharmacol. Ther.* **95,** 21–45 (2002).